Remote Sensing of Environment 268 (2022) 112758

Contents lists available at ScienceDirect

Remote Sensing of Environment

journal homepage: www.elsevier.com/locate/rse

First multi-year assessment of Sentinel-1 radial velocity products using HF radar currents in a coastal environment

Adrien C.H. Martin [a,*], Christine P. Gommenginger [a], Benjamin Jacob [b], Joanna Staneva [b]

[a] National Oceanography Centre, European Way, Southampton SO14 3ZH, United Kingdom
[b] Helmholtz-Zentrum hereon GmbH, Max-Planck-Straße 1, 21502 Geesthacht, Germany

ARTICLE INFO

Edited by Dr. Menghua Wang

Keywords:
Total ocean surface current
Sentinel-1
Doppler
SAR
WASV
Sea state
Coastal circulation
HF radar

ABSTRACT

Direct sensing of total ocean surface currents with microwave Doppler signals is a growing topic of interest for oceanography, with relevance to several new ocean mission concepts proposed in recent years. Since 2014, the spaceborne C-band SAR instruments of the Copernicus Sentinel-1 (S1) mission routinely acquire microwave Doppler data, distributed to users through operational S1 Level-2 ocean radial velocity (L2 OCN RVL) products. S1 L2 RVL data could produce high-resolution maps of ocean surface currents that would benefit ocean observing and modelling, particularly in coastal regions. However, uncorrected platform effects and instrument anomalies continue to impact S1 RVL data and prevent direct exploitation.

In this paper, a simple empirical method is proposed to calibrate and correct operational S1 L2 RVL products and retrieve two-dimensional maps of surface currents in the radar line-of-sight. The study focuses on the German Bight where wind, wave and current data from marine stations and an HF radar instrumented site provide comprehensive means to evaluate S1 retrieved currents. Analyses are deliberately limited to Sentinel-1A (S1A) ascending passes to focus on one single instrument and fixed SAR viewing geometry. The final dataset comprises 78 separate S1A acquisitions over 2.5 years, of which 56 are matched with collocated HF radar data. The empirical corrections bring significant improvements to S1A RVL data, producing higher quality estimates and much better agreement with HF radar radial currents.

Comparative evaluation of S1A against HF radar currents for different WASV corrections reveal that best results are obtained in this region when computing the WASV with sea state rather than wind vector input. Accounting for sea state produces S1 radial currents with a precision (std of the difference) around 0.3 m/s at ~1 km resolution. Precision improves to ~0.24 m/s when averaging over 21 × 27 km^2, with correlations with HF radar data reaching up to 0.93. Evidence of wind-current interactions when tides and wind align and short fetch conditions call for further research with more satellite data and other sites to better understand and correct the WASV in coastal regions.

Finally, 1 km resolution maps of climatological S1A radial currents obtained over 2.5 years reveal strong coastal jets and fine scale details of the coastal circulation that closely match the known bathymetry and deep-water coastal channels in this region. The wealth of oceanographic information in corrected S1 RVL data is encouraging for Doppler oceanography from space and its application to observing small scale ocean dynamics, atmosphere and ocean vertical exchanges and marine ecosystem response to environmental change.

1. Introduction

The possibility of measuring ocean surface motion directly from Doppler shifts in microwave radar signals has been known for many years (e.g. Shuchman and Meadows, 1980; Rufenach et al., 1983; Goldstein and Zebker, 1987; Plant and Alpers, 1994) and has since been demonstrated many times from fixed, airborne and satellite systems, both with the Doppler Centroid Anomaly (DCA) and Along-Track Interferometry (ATI) methododologies. More recent examples based on spaceborne Envisat-ASAR (Chapron et al., 2005), TerraSAR-X and Tandem-X SAR data (Romeiser et al., 2010, 2014) have stimulated renewed interest in the capabilities of ocean Doppler signals to measure ocean surface currents from space. The large and stable Envisat satellite platform led to significant progress in understanding the geophysical

* Corresponding author.
E-mail address: admartin@noc.ac.uk (A.C.H. Martin).

https://doi.org/10.1016/j.rse.2021.112758
Received 5 January 2021; Received in revised form 2 October 2021; Accepted 15 October 2021
Available online 30 October 2021

information contained in ASAR Doppler signals, opening up promising new opportunities for oceanographic applications (Johannessen et al., 2008; Rouault et al., 2010; Hansen et al., 2011). As the prospect of accurate measurements of Doppler signals from space gains maturity, a wealth of satellite mission concepts are emerging to measure ocean surface currents. Amongst those, WaCM (Rodríguez et al., 2019) and SKIM (Ardhuin et al., 2019) Doppler scatterometry concepts propose global daily mapping of surface current vectors for atmosphere-ocean coupling applications, whereas ATI-based concepts like SEASTAR (Gommenginger et al., 2019) would measure ocean surface current fields with greater accuracy and much finer spatial resolution (1 km) to study small-scale upper ocean dynamics and vertical exchanges with the ocean interior in coastal, shelf and polar seas. Given the growing interest in Doppler from space, it is relevant therefore to review the capability available today and its usefulness to observe ocean currents.

The Copernicus Sentinel-1 (S1) mission (Torres et al., 2012) delivers all-weather global observations with active microwave Synthetic Aperture Radar (SAR) payloads operating at C-band that build on strong heritage from Envisat-ASAR. The S1 mission comprises two units, currently Sentinel-1A (S1A) and Sentinel-1B (S1B), both orbiting in sun-synchronous orbits with an exact repeat of 12 days. S1A was launched on April 3, 2014 and S1B on April 25, 2016. S1 instrument operates in different modes over different regions, characterised by different spatial resolutions and image sizes driven by operational user needs. Over European waters, the default acquisition mode is Interferometric Wide swath (IW) mode, with stated minimal requirements for a 250 km swath in three sub-swaths and 5×20 m spatial resolution at Level-1 (Torres et al., 2012). In IW, S1 uses the Terrain Observation with Progressive Scans (TOPS) SAR acquisition to mitigate some of the drawbacks of conventional Scan SAR mode (De Zan and Monti Guarnieri, 2006). This study uses S1 IW Level-2 products acquired with TOPS SAR mode.

Operational S1 Level-2 products are processed and disseminated by the European Space Agency (ESA). S1 Level-2 IW Ocean products (Level-2 OCN) consist of two sub-products: Ocean Wind field (OWI; spatial resolution of 1×1 km^2) and surface radial velocity (RVL; spatial resolution of 0.9×0.7–0.8 km^2). RVL products contain the S1 Doppler data. Level-2 Ocean Swell spectra (OSW) are not currently available operationally for S1 IW mode.

It is now widely acknowledged that operational S1 Level-2 RVL products suffer from significant uncorrected platform and instrument effects that presently prevent direct exploitation of the data for science and applications (Moiseev et al., 2020b; Hajduch et al., 2021). For this reason, even though S1A has been flying for over six years, the operational Level-2 RVL products are generally unused. To the best of our knowledge, only one study (Moiseev et al., 2020a) used operational S1 IW data to infer ocean surface currents, albeit with specialised Level-0 to Level-2 processed data rather than operational S1 Level-2 products.

In contrast, this paper considers S1 ocean surface currents starting from operational S1 Level-2 RVL products. A simple empirical method is proposed to correct operational RVL products for platform-related biases, and the geophysical information content of the new S1 Level-2 RVL data is subsequently evaluated against ground-based data. The study focuses on the German Bight, a highly dynamic region where the ocean circulation is strongly influenced by physical drivers such as tides, wind, waves and river forcing. The region is instrumented with an HF radar system and a good network of in-situ monitoring stations. The German Bight HF radar data have been used extensively in previous studies to validate high-resolution coastal models and for data assimilation (Barth et al., 2010). S1 Level-2 RVL products are processed for a specific S1A acquisition geometry (ascending passes only) every 12 days over a period of 2.5 years, resulting in 78 snapshots over the HF radar instrumented site in the German Bight.

A second consideration in this paper concerns the wave bias correction to be applied to spaceborne Doppler velocity data. Microwave radars sense directly the motion of the ocean surface in the line-of-sight of the radar. This motion includes all ocean currents associated with an effective horizontal transport of mass (e.g. geostrophic and tidal currents, wind drift and surface wave Stokes drift, etc.) and a wave induced bias related to microwave scattering (Chapron et al., 2005; Martin et al., 2016). This wave bias, also known as the Wind-wave induced Artefact Surface Velocity (WASV), is related to the phase velocity of the surface scatterers responsible for the microwave backscatter (e.g. Bragg waves) and the orbital motion of longer ocean waves (Figure 6 in Chapron et al., 2005). The WASV can bias measured currents by up to 2 m/s with the potential to obscure all but the strongest sea surface currents unless appropriate correction is applied.

The first empirical model put forward to estimate the WASV was developed for Envisat-ASAR (Mouche et al., 2012). The WASV correction is a function of incidence angle and wind, with first-order dependency on wind direction (positive bias downwind, negative upwind, low values crosswind). An updated model was recently developed for Sentinel-1 Wave mode (WV) data (Moiseev et al., 2020b) that parameterises the WASV either by wind alone or with more comprehensive sea state descriptions. At time of writing, this model is not publicly available for independent evaluation.

Many other models have been proposed over the years, typically derived from theoretical models of microwave scattering (e.g. Romeiser and Thompson, 2000; Nouguier et al., 2011; Fois et al., 2015). Another model is the semi-empirical formulation proposed by Yurovsky et al. (2019) that was derived from a wide range of observations from an oceanographic platform in the Black Sea. This model, which parameterises the WASV by either wind or sea state, shows very good agreement with many historical observational datasets at different radar frequencies. The Mouche et al. (2012) and Yurovsky et al. (2019) models will be explored in this paper to examine how well they mitigate the WASV in S1 RVL data.

The paper is organised as follows: a description of the data used is presented in Section 2. Section 3 presents the details of the different corrections that have been developed and applied to mitigate platform-related issues in S1 Level-2 RVL products. In Section 4, the corrected S1 RVL data are assessed against coincident HF radar measurements for different WASV corrections. The discussion of these results is found in Section 5, followed by conclusion and outlook in Section 6.

2. Data

2.1. Sentinel-1 data

The study focuses on S1 data over the German Bight region where land is imaged by the radar instrument in both across-track and along-track directions (Fig. 1). The S1 RVL data correspond to snapshots obtained with S1A in the exact same geometry (S1A ascending) in IW acquisition mode. The same geometry occurred exactly every 12-days, resulting in a total of 78 S1A overpasses between 01 December 2017 and 06 July 2020. No S1A data before December 2017 were used in order to benefit from the improved satellite attitude orbit control system after that date. In this study, the Sentinel-1 dataset deliberately omits data from S1A descending passes and S1B to limit potential sources of discrepancy and focus on a single satellite, single instrument and single acquisition geometry for the empirical land-based correction approach we propose.

2.1.1. Level-2 RVL and OWI normalised radar cross-section

The S1 Level-2 RVL products have a spatial resolution $\approx 1 \times 1$ km (0.7–0.8 km in range, 0.9 km in azimuth). The 250 km swath is composed of three sub-swaths that span incidence angles between [30°–36°] (near-swath), [36°–42°] (mid-swath) and [41°–46°] (far-swath). Fig. 1 presents an example of operational S1 Level-2 OWI and RVL products acquired on 15 September 2018 at 17h10, showing (Fig. 1A and B) OWI Normalised Radar Cross-Section (NRCS) for VV co-polarisation and VH cross-polarisation respectively, and (Fig. 1C) RVL

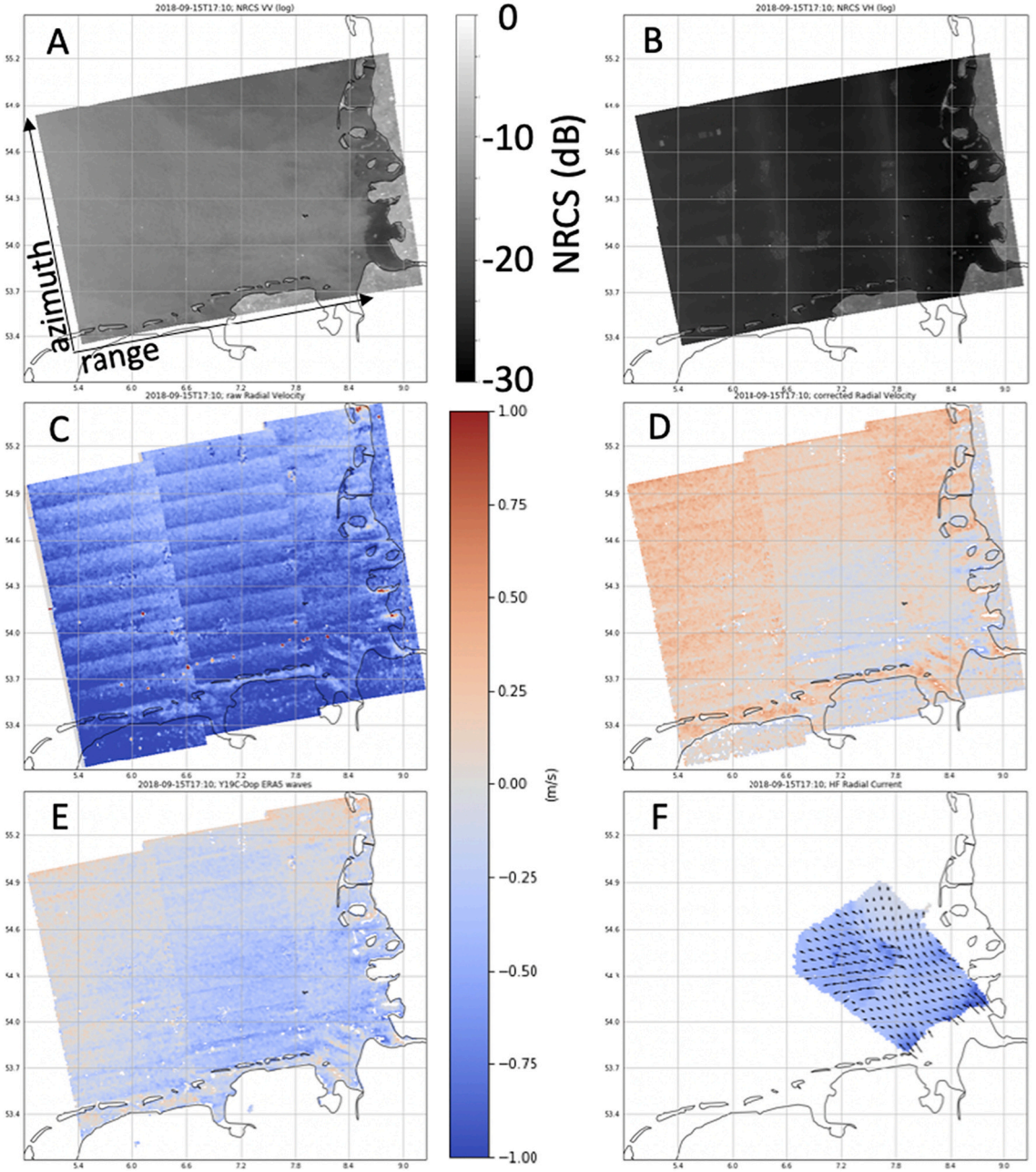

Fig. 1. Sentinel-1A acquisition over the German Bight on 15 September 2018 (17h10): (A) Co-polarised Normalised Radar Cross Section (NRCS) in dB from operational Level-2 OCN OWI product; (B) Cross-polarised NRCS (dB) from operational Level-2 OCN OWI product; (C) Radial velocities from operational Level-2 OCN RVL product; (D) Corrected radial velocities after scalloping and land-based corrections; (E) Radial currents after all corrections including WASV (Y19C-Dop ERA5 waves); (F) Radial current in the S1 line-of-sight measured by HF radar. Grayscale bar shows dB for (A) and (B). Colour bar shows m/s for (C) to (F). S1A is ascending, looking right. (For interpretation of the references to color in this figure legend, the reader is referred to the web version of this article.)

radial velocity. Near-range corresponds to the South-Western edge of the scene and far range to the North-East part. The radial velocity is measured in the radar line-of-sight (range) perpendicular to the satellite flight direction (azimuth, also known as along-track).

Away from the coast, the co-polarised VV NRCS (Fig. 1A) presents a seamless homogeneous scene with no imaging artefacts, showing faint large scale imprints indicative of fronts and instabilities in the atmospheric boundary layer. For this acquisition, the wind ranged between 5 to 10 m/s from West to North-West and the tide was ebbing. Close to the Elbe river mouth (South-East corner), a region of low backscatter is clearly noticeable, possibly linked to emerging sand banks at low tide. The cross-polarised VH NRCS scene (Fig. 1B) is also mostly uniform, and as expected, VH NRCS values are much smaller (darker) over the ocean than VV NRCS. Geometric features that stand out over the ocean in the VH data (Fig. 1B) are the large wind farms in the middle of the Bight. Two mid-scene brighter bands in the along-track direction are linked to the edges of the sub-swaths.

The original S1 operational RVL product (Fig. 1C) shows well-marked sub-swath edges parallel to the satellite track, as well as striking repeated wavy patterns in the azimuth direction. These patterns are recognised as scalloping linked to the TOPS acquisition technique (Rodriguez-Cassola et al., 2015) and have no geophysical meaning. The RVL values are typically strongly negative (dark blue) over the full scene, including over land. Whereas it is difficult to know a-priori the value of RVL over ocean, over land, because land is static, we expect RVL values around zero on average, which is far from being the case in this

example. This bias in RVL has been traced back to anomalies in the S1 Attitude and Orbit Control System (AOCS) when calculating the Doppler Centroid (DC) frequency (Hajduch et al., 2021). In addition, some IW data are impacted by sudden jumps in DC from one burst to another that impact RVL and persist over all swaths. Hajduch et al. (2021) reports these jumps are linked to on-board temperature compensation. No correction or flagging of these jumps is provided so far at Level-2.

Beyond the platform-related biases and scalloping effects, strong outliers are also visible in the RVL scene (Fig. 1C), showing up as red points. Some of these outliers also appear as bright targets in the co- and cross-polarised NRCS scenes (Fig. 1A and B). These are mainly related to human-made structures like ships, fixed platforms and wind farm installations. No flagging of these outliers is provided in Level-2 RVL product. An outlier flagging algorithm was developed and applied to all RVL data and is described in Section 3 "Sentinel-1 RVL corrections".

2.1.2. Level-2 OWI wind

Sentinel-1 Level-2 OWI products contain two estimates of the ocean surface vector wind at 10 m above the sea surface (Mouche et al., 2019): the wind speed and direction from the European Centre for Medium-Range Weather Forecasts (ECMWF) atmospheric model forecast, provided with spatial and temporal resolutions better than 0.25 degrees and 3-hourly (Bourbigot et al., 2020); and a wind speed and direction retrieved from S1 NRCS and a priori wind from the previous ECMWF forecast using a Bayesian approach. The mean bias between S1A Bayesian wind speed and ECMWF forecast ranges between −0.04 and 0.11 m/s with a root-mean-square difference of ~1.5 m/s (Hajduch et al., 2021). S1 wind direction is very similar to ECMWF wind direction except at low wind speeds [0–5 m/s] where performance degrades when the S1 radar looks crosswind (Hajduch et al., 2021, Fig 64a).

2.2. HF radar data

The surface currents ground-truth data used to validate S1 RVL stem from three High Frequency (HF) Wellen Radar stations (WERA, Gurgel et al., 1999) around the German Bight, which run pre-operationally in the framework of the Coastal Observing System for Northern and Arctic Seas (COSYNA, Baschek et al., 2017). The three stations are located on the islands of Sylt and Wangerooge, and on the mainland near Büsum (marked as black dots in Fig. 2 and respectively labeled as HFS, HFW and HFB). The HF radar installation covers a 120° field of view with a spatial resolution of 3° in azimuth and 1.5 km in range.

The radar on Wangerooge operates at 12.1 MHz with a 16 antennae array, while the other two stations operate at 10.8 MHz with an array of 12 antennae. The radar interacts with ocean waves of 12.5 m (12.1 MHz) and 13.9 m (10.8 MHz) length scales via Bragg scattering, providing information about surface currents in the top 1 m of the water column (Stewart and Joy, 1974; Teague et al., 2001; Stanev et al., 2015).

The system provides hourly measurements and the radial components of ocean surface currents are retrieved as averages over 20 min. The HF radar data span a range of typically 100 km depending on environmental conditions (e.g. sea state, salinity), electromagnetic noise and radar frequency (maximum achieved range is 150 km). After transmission of the data to the main server at Hereon, quality control is applied and surface current vector fields are computed. By combining the radial current components measured from the different stations, meridional and zonal current components are derived, yielding Cartesian velocity fields with a grid resolution of about 2 km. Further details about the system can be found in Stanev et al. (2015). The HF-radar data are available through COSYNA (see full details in Baschek et al., 2016).

The validation of S1 RVL measurements used only HF radar data available within a tolerance window of ±20 min from the satellite overpass, using the HF radar observation closest in time (for some acquisitions no HF radar data were available). Analyses compared the S1 RVL against the component of the HF currents obtained by projecting the Cartesian velocity fields in the line-of-sight of S1.

A measurement accuracy limit was imposed on the HF radar data to ensure that only the best HF radar data were used in the comparisons with S1. The HF radar measurement accuracy is an output of the HF radar processing. It depends on viewing geometry (worse accuracy at edges of HF radar field of view) and environmental conditions. In this study, only HF radar data with accuracies in the S1 line-of-sight direction better than 90% were used, corresponding to an accuracy limit of 0.09 m/s. The median accuracy of the HF radar data is 0.04 m/s.

The spatial distribution of the number of match-ups between S1 and high-accuracy HF radar data is presented in Fig. 2A. For completeness, Fig. 2B and C show the median surface current fields measured by the HF radar during Flood and Ebb tidal conditions at the time of S1 acquisitions. Over the whole domain, the HF radar current has a median speed of 0.40 m/s, with weaker currents offshore (0.30 m/s) and stronger currents near the coast. The currents differ most markedly between tidal Flood and Ebb at the coast. The strongest currents (95th percentile) are 0.52 m/s during Flood, and even stronger during Ebb (0.70 m/s).

Recalling that S1 can only sense the current component along its line-of-sight (across-track), a current directed towards S1 will result (typically during Ebb) in a negative S1 radial current.

2.3. Wind and wave model data

2.3.1. ERA5 wind and wave data

Wind and waves data are taken from the ERA5 global reanalysis (Hersbach et al., 2020) with hourly outputs. Wind speed and direction are derived from the 10 m zonal and meridional component of the neutral wind and are re-gridded on S1 RVL grid for the closest data in time. Original ERA5 grid for wind is a regular 0.25° grid.

ERA5 waves statistical moments of wind sea and swell for direction, significant wave height and frequency are provided on a regular 0.5° grid, hourly and are re-gridded on S1 RVL grid.

2.3.2. Hereon wave model data

The spatial wave information used to correct S1 data for the WASV stems from the wave component of the operational Geestacht COAstal model system, GCOAST (Staneva et al., 2021). Within this system, the WAM wave model (Group, 1988) is two-way coupled with the NEMO (Nucleus for European Modelling of the Ocean) hydrodynamic model to represent nonlinear wave ocean interactions. WAM is an advanced state-of-the-art spectral wave model that solves the wave action equation without a priori assumption on wave spectrum evolution. The consideration of depth refraction and wave breaking make it suitable for coastal applications in regions such as the German Bight. The model wave spectra are discretized on a polar grid with 24 directional bins (15°) and 30 frequencies logarithmically spaced between 0.042 and 0.66 Hz. The spatial domain covering the North Western European shelf is resolved with a spherical grid with a resolution of ~0.06°(~0.03°) in zonal (meridional) direction. The wave model is driven by atmospheric wind forcing from ECMWF ERA5, and wave boundary conditions from a coarser (0.25°) WAM configuration for the entire North Atlantic. Earlier validations of WAM and GCOAST models in configurations similar to those used here demonstrated very good performance against in-situ measurements of significant wave height (see e.g. Figure 2f of Wiese et al. (2018) showing bias/RMSE/correlation ≈0.06 m/0.31 m/0.96).

2.4. In situ wind and wave data

The in situ wind and wave measurements were obtained from weather stations and wave buoys located in and around the German Bight. In situ wind data was obtained for 13 stations operated by the German Weather Service (Deutscher Wetterdienst, DWD) that can be accessed via their climate data center (https://www.dwd.de/EN/ourservices/cdc_portal/cdc_portal.html). The positions of the individual stations are indicated in Fig. 2A as red dots labeled by station number. Three stations of particular interest in this study are UFS Deutsche Bucht

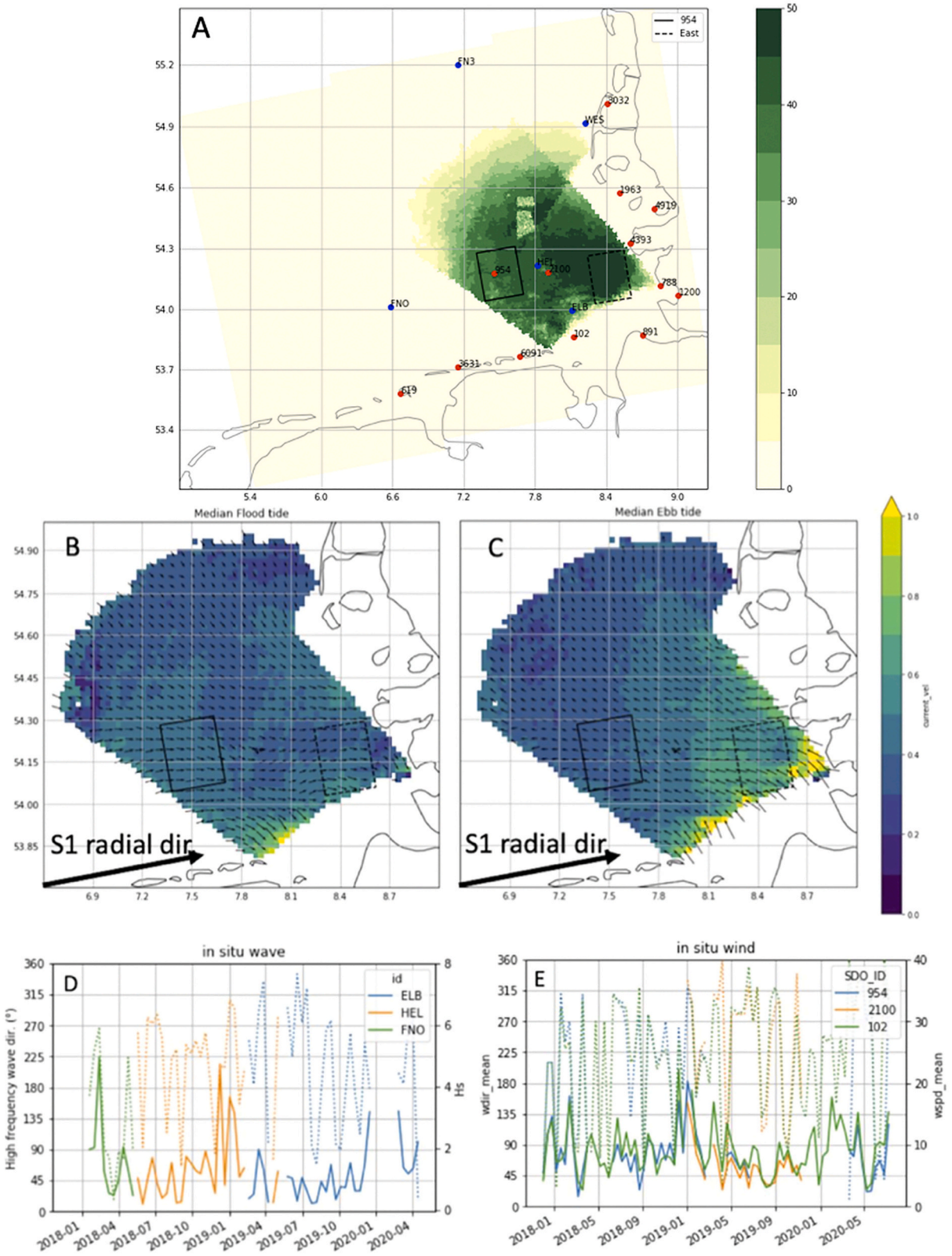

Fig. 2. Study area over German Bight: (A) S1 coverage (beige) and distribution of S1/HF radar match-ups (green colours). Blue and red dots indicate the positions of in situ wave and wind measuring instruments. Black dots show the three HF radar stations. The two rectangles are 30 × 30 pixels denoted as (solid line) Box 954 and (dashed line) East Box. (B) and (C) Median HF radar currents as sampled by S1 during flood and ebb tide. (D) in situ wave height (solid) and direction (dashed) at stations ELB, HEL and FNO for S1 overpasses. (E) in situ wind speed (solid) and direction (dashed) at stations 954, 2100 and 102 for S1 overpasses. Both (D) and (E) assume meteorological convention for wind and wave direction ("coming from"). (For interpretation of the references to color in this figure legend, the reader is referred to the web version of this article.)

(954), Helgoland-Düne (2100) and Leuchtturm Alte Weser (102). In situ wind information is available as hourly averages of wind speed and direction at 10 m height, measured either via an Ultrasonic Anemometer or a combination of electro-mechanical sensors for wind speed and direction, depending on the station. Wind direction data are rounded to every 10°. Wind speed and direction at stations 102, 2100 and 954 at the time of the S1A overpasses are presented in Fig. 2E.

In situ wave information is available as spectral and integral wave parameters obtained from five Waverider buoys operated by the Federal Maritime and Hydrographic Agency (Bundesamt für Seeschifffahrt und Hydrography, BSH)) as part of the Marnet-network (Marines Meeresumweltmessnetz zur Überwachung der Meeresumwelt, https://www.bsh.de/DE/THEMEN/Beobachtungssysteme/Messnetz-MARNET/messnetz-marnet_node.html). The locations of the buoys are indicated in Fig. 2A as blue dots. Three sites of particular interest here are Elbe (ELB), Fino 1 (FNO) and Helgoland-Nord (HEL). Significant wave height and mean direction of waves with periods shorter than 0.5 s at the time of S1A overpasses are presented in Fig. 2D.

2.5. Bathymetry

High-resolution bathymetry data describing the sea floor morphology of the German Bight help to relate dynamic signatures in remote sensing data to underwater topographic features (i.e. increased velocities in pronounced tidal channels) and support the interpretation of observed current structures. The dataset used here is the 2016 bathymetry of the German Bight, obtained as GeoTiff together with the meta data from the EasyGSH-DB Portal (Bundesanstalt für Wasserbau et al., 2019) operated by the Bundesanstalt für Wasserbau (BAW; Federal Institute for Hydraulic Engineering). The bathymetry data originates from various types of measurements (profiles, echo sounding, lidar, historic maps, etc.), which were compiled and integrated in an operational sea floor model (Milbradt et al., 2015) combining process based modeling and spatio-temporal data interpolation methods. The resulting rasterized data have a resolution of 10 m and are distributed as annual bathymetry products (1996–2016). Over the German Bight area, the products cover an area with a landward reach of 200 m beyond the dike line (Fig. 5C).

3. Sentinel-1 RVL corrections

3.1. Overview

Sentinel-1 RVL data need to be corrected for non-geophysical anomalies which significantly impact SAR Doppler signals contained in operational RVL Level-2 products(Fig. 1C). A sequence of corrections is proposed to mitigate these issues and improve the quality of S1 RVL data.

First, outliers originating mainly from ships and human-made structures in the SAR scenes are flagged and removed based on statistical distribution. Next, corrections of the scalloping effect linked to TOPS mode is applied.

At this stage, S1 RVL data will generally show strong residual biases affecting the full scene. The example in Fig. 1C shows S1 RVL with average velocity values around −0.5 m/s over land (East and South parts of the image), which contradicts the expectations of velocity values around zero over land. This anomalous bias over land has two main causes (Hajduch et al., 2021):

- S1 satellite navigation and attitude errors: this effect will be particularly evident in the along-track (azimuth) direction and should have similar signatures in all sub-swaths. Some similarity between overpasses may exist (as they correspond to the exact same portion of the orbit) but the effect is expected to differ in different snapshots;
- Antenna electronic mispointing: this effect will be constant for all scenes and is expected to present a linear variation with range (across-track) within each sub-swath;

Other errors in operational S1 RVL products include jumps in RVL. These jumps are associated with unexplained changes in instrument gain. They are not presently flagged at Level-2 and are therefore not easy for users to detect and remove. These jumps occur in the along-track direction over distances that correspond to integer numbers of wave scalloping patterns. The errors affect the separate sub-swaths independently. So far, no correction or flags exist to mitigate the impact of these RVL jumps.

Finally, once RVL data have been corrected for these satellite and instrument-related effects, a further correction for wave bias (WASV) needs to be applied to convert S1 radial *velocities* into radial *currents* that can be compared with independent validation data. The correction of the WASV is presented in Section 3.3 “Wind-wave artefact surface velocity correction”.

3.2. Geometrical corrections to S1 RVL

3.2.1. Pre-processing outliers flagging

Outliers in the RVL data are detected and flagged in each S1 snapshot separately. Outliers are identified first in the range direction (across-track) then along azimuth (along-track) for each sub-swath, before being combined. In each case, a pixel is flagged as an outlier if the value departs from the median RVL by more than three robust standard deviations, where the median and standard deviation refer to either range or azimuth directions (Eq. (1))

$$\begin{aligned} &\text{Outlier}_{\text{range}} \ \text{ if : } \ |x - \widetilde{x}_{\text{range}}| > 3\sigma_{\text{range}} \\ &\text{Outlier} = \text{Outlier}_{\text{range}} \ \cup \ \text{Outlier}_{\text{azimuth}} \end{aligned} \tag{1}$$

For robust estimation, the standard deviation is estimated from the data distribution as 1.48 times the Median Absolute Difference (MAD). The flagged data are excluded from all further analyses.

3.2.2. De-scalloping

The wavy patterns seen in each sub-swath in Fig. 1C, known as scalloping, are consistent between S1 scenes. However, each sub-swath has its own pattern. The scalloping that modulates the RVL is easily estimated by taking a range-average in each sub-swath (Fig. 3A) that is then removed from the data. The modulation is periodic along-track and has an amplitude of about 0.1 m/s. As of 24 June 2020, the S1 Instrument Processing Facility version 3.30 (IPF) includes a correction of the azimuth scalloping that reduces the modulation by a factor of 3 (Hajduch et al., 2021).

3.2.3. Antenna electronic mispointing correction

RVL variations with range are primarily due to antenna electronic mispointing. To correct this problem, only RVL pixels over land in each image are used, based on the S1 land flag information provided in the RVL products. For each image, the median RVL of land pixels at each range position is calculated along the azimuth direction. Fig. 3B shows the azimuth-median RVL anomaly against range, the different colours representing each of the 78 snapshots. The black curve is the median of all coloured curves, and the black line is the least-square linear fit of the black curve for each of the three sub-swaths.

The figure clearly shows the three sub-swaths and the linear evolution of the error with range within each sub-swath. The solid black line for each sub-swath is chosen to represent the correction to RVL of the mean uncorrected antenna electronic mispointing. This correction is applied to the full image (land + ocean) for each snapshot. The correction has values from −0.4 m/s at near range to +0.1 m/s at far range. At some ranges, there are very few observations over land which could explain some of the large pixel-to-pixel variability seen in Fig. 3B.

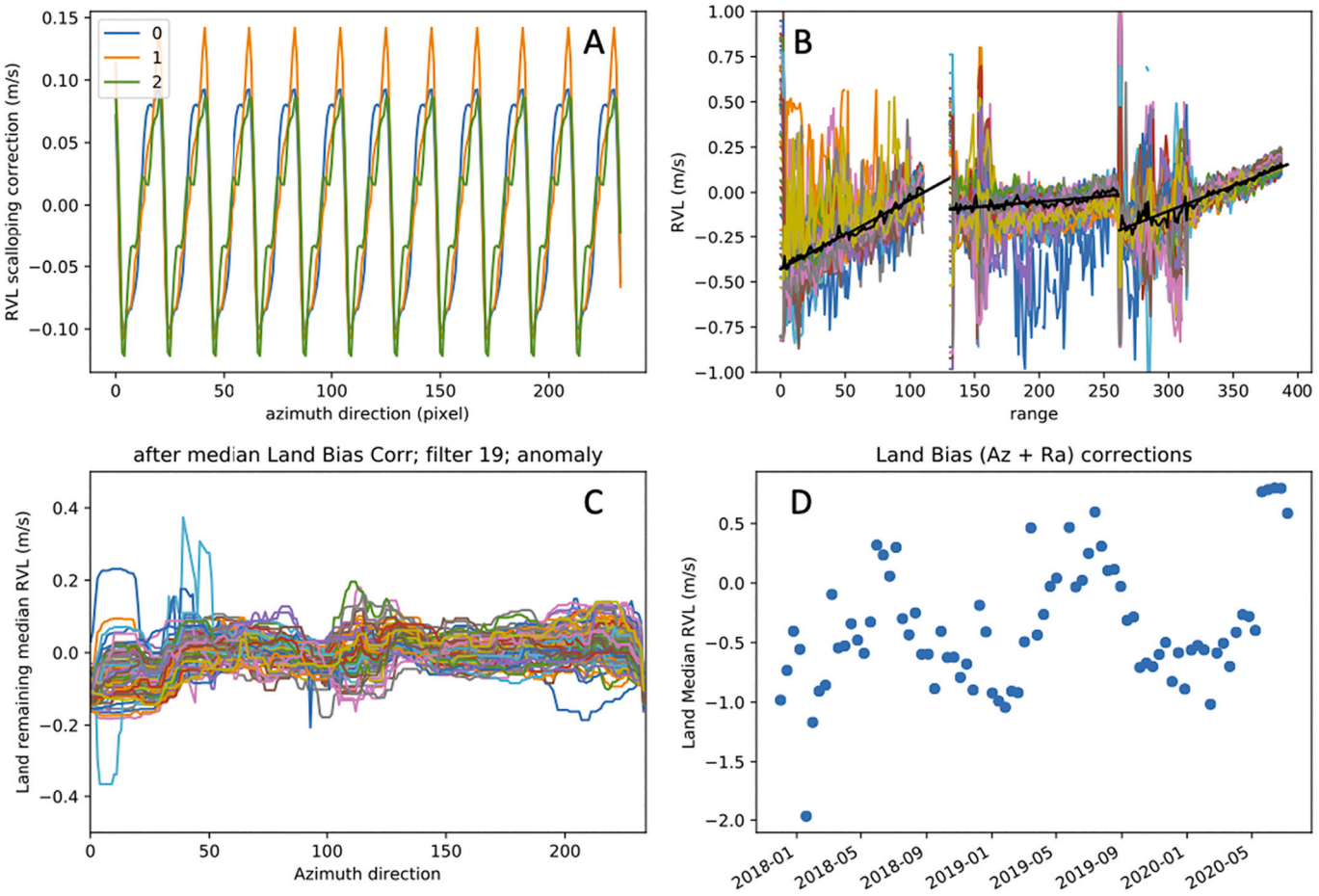

Fig. 3. S1 RVL anomalies and corrections: (A) Scalloping along azimuth in the near (0, blue), mid (1, orange) and far (2, green) sub-swaths averaged over 78 S1 passes. (B) Azimuth-median RVL anomaly against range. Range is measured relative to the nearest edge of the near-swath. Colours represent 78 different S1 passes. The RVL median value has been removed from each pass to show anomalies only. The black curve is the median of all coloured curves. The black line is the least-square linear fit of the black curve in each sub-swaths. (C) Range-median RVL anomaly against azimuth for the eastern sub-swath. Zero azimuth corresponds to the southern part of the S1 scene in Fig. 1C. Colours represent 78 different S1 passes. Data were filtered with a 19-pixels along-track median filter. (D) Time-series of median RVL over land for 78 S1 passes. (For interpretation of the references to color in this figure legend, the reader is referred to the web version of this article.)

3.2.4. *Platform navigation and attitude errors*

Using again only pixels over land, we now calculate the median RVL at every azimuth position in the range direction (across-track). We show the range-median RVL anomaly in Fig. 3C for the 78 snapshots, this time plotted against azimuth. Data are smoothed using a median filter (19 pixels) to remove some of the strongest variability not related to attitude errors. The 19-pixel filter is chosen to fit just within the 21-pixels of the scalloping pattern. In Fig. 3C, some consistency is observed in the azimuth patterns of different snapshots, probably due to the impact of similar orbital conditions on RVL in the same part of the orbit. The anomaly generally varies within ±0.2 m/s. This correction is applied to the full image (land + ocean) for each snapshot.

Finally, we consider the median RVL values over all land pixels (rather than anomalies) for each snapshot. This is shown in Fig. 3D. The temporal variation of the median RVL is by far the largest discrepancy between different scenes. These biases, thought to originate from uncorrected platform attitude effects, can range from −2.0 m/s to +0.8 m/s. Note the marked seasonal variation in the RVL bias, with maximum (minimum) values coinciding with North Hemisphere summer (winter) solstice. The median RVL bias is removed by applying it to the full image for each snapshot.

3.2.5. *Corrected radial velocity measurements*

The impact of applying these empirical corrections for scalloping, mispointing and navigation/attitude errors is illustrated in Fig. 1D for a specific S1A example. At this point, the values correspond to 'corrected radial velocities' ('cor RV'), not yet currents (see next section). As expected, after the satellite and instrument corrections have been applied, the mean cor RV over land is zero.

The strong scalloping previously seen in Fig. 1C is now much reduced, although some residual oscillations that follow the original wavy patterns still remain, indicating that the pattern is not perfectly constant in time, from scene to scene.

Over the ocean, cor RV is now positive or zero (Fig. 1D) rather than strongly negative (Fig. 1C). If the signals responded solely to ocean currents, this would indicate currents flowing. However, HF radar data at the time of the S1 overpass (Fig. 1F) indicate an ebbing tide with currents westwards towards the radar. In the next section, we introduce the Wind-wave Artefact Surface Velocity (WASV), a wind-wave bias correction that has to be applied to any microwave radar Doppler measurements to convert radial *velocities* into radial *currents* that can be compared with other ocean surface current measurements.

3.3. *Wind-wave artefact surface velocity correction*

Microwave radar Doppler measurements are strongly affected by the motion of the ocean surface scatterers responsible for the radar backscatter. This velocity is related to short capillary waves (Bragg scatterers) and their modulation by longer ocean wind waves (e.g. Chapron et al., 2005; Martin et al., 2016). It is an unwanted bias caused by

microwave scattering that has to be removed from the radar Doppler signals. This wind-wave artefact surface velocity (WASV), also sometimes called wave bias, can be up to 2 m/s and will obscure the real ocean surface currents unless correctly removed.

To first order, the WASV is a function of the relative direction between the surface wind (or wind waves) and the radar line-of-sight, and to second order, of incidence angle and wind speed. The amplitude of the wave bias is largest in the up/downwind directions. One of the earliest models of the WASV was proposed by Mouche et al. (2012) based on an empirical formulation developed using global open-ocean Envisat ASAR data. This model is henceforth denoted as M12C-Dop.

More recently, a semi-empirical model was developed by Yurovsky et al. (2019) using a large dataset of observations from a Ka-band radar located on an oceanographic platform in the Black Sea. Although the model was developed from Ka-band Doppler measurements, the model showed excellent agreement with a wide range of Doppler measurements published in literature from different radar systems, different radar frequencies and different ocean and environmental conditions. The model is applicable to C-band data and is denoted as Y19C-Dop in the rest of the paper.

Both M12C-Dop and Y19C-Dop need input about the acquisition geometry (incidence angle, azimuth look direction) and environmental conditions (wind or sea state). Environmental input for M12C-Dop are the wind speed and wind direction. For Y19C-Dop, the model input consists of various spectral parameters of sea state. By default, Y19C-Dop assumes fully developed sea conditions (Pierson and Moskowitz, 1964) based on input wind speed and wind direction. But Y19C-Dop can also be driven directly with sea state parameters, including wind sea significant wave height, peak frequency and direction, and the same for swell.

The WASV correction was computed using M12C-Dop and Y19C-Dop for the 78 S1A scenes over German Bight. Various sources of wind and sea state input were tested, using validation against HF radar currents to evaluate performance. Wind data are taken either from the operational S1 Level-2 OCN OWI wind products (noted, S1 winds) or from ERA5 (noted, ERA5 winds). Sea state data are taken from the high-resolution Hereon numerical wave model (noted, Hereon waves) or from ERA5 (noted, ERA5 waves). Unless mentioned otherwise, the Y19C-Dop model uses both wind sea (mean direction, significant wave height and frequency) and total swell (mean direction, significant wave height and frequency) as input.

Fig. 1E shows an example of the impact of the WASV correction on S1 Doppler data. At this point, all corrections and the WASV have been applied to the S1 radial velocities ('cor RV') and the values shown are corrected radial currents ('cor RC'). In this particular example, the WASV is estimated using Y19C-Dop with ERA5 waves as input.

The impact of the WASV is striking. On the day shown in Fig. 1, the wind is blowing from the West, close to a downwind direction for S1. The WASV as estimated by Y19C-Dop is about +0.3 m/s. Without the WASV correction (Fig. 1D), the S1 corrected radial velocities are generally positive (eastwards). After the WASV is applied (Fig. 1E), S1 radial ocean surface currents are generally negative (westwards, towards S1). This westward current field is more consistent with the ebb phase of the tide observed with the HF radar measurements (Fig. 1F), confirming the importance of accounting for the WASV when retrieving surface currents from microwave radar data.

4. Results

The corrections described in the previous section were applied to all 78 Sentinel-1A scenes obtained over German Bight during the study period. S1 overpasses were time-matched with HF radar observations within a ±20 min time window, resulting in a reduced dataset of only 56 match-ups. All 56 S1A and HF radar current fields in the match-up

Table 1
Statistics of S1 radial velocities (RV) and radial currents (RC) versus HF radar for: (A) Corrected RC with Y19C-Dop(ERA5 waves) over (all colloc/full) all collocated S1/HF points over the full domain, (all colloc/boxes) all collocated points within given boxes, (median/boxes) median values within given boxes; (B) Median values in Box 954 for different RC, RV and WASV corrections; (C) same for Box East. Columns show: number of available samples (*N*); mean and median bias; standard deviation (std); median absolute deviation (mad); rms difference (rms); and Pearson correlation coefficient (*r*).

(A) CORRECTED RC with Y19C-Dop(ERA5 waves)

		N	mean	median	std	mad	rms	*r*
All colloc	Full domain	551,725	0.00	0.00	0.29	0.23	0.29	0.73
All colloc	Box 954	38,898	-0.07	-0.05	0.25	0.20	0.26	0.80
	Box East	42,626	0.09	0.10	0.30	0.24	0.31	0.83
Median	Box 954	50	-0.08	-0.05	0.23	0.20	0.25	0.84
	Box East	50	0.09	0.11	0.24	0.20	0.26	0.93

(B) MEDIAN over BOX 954

S1	WASV	*N*	mean	median	std	mad	rms	*r*
Raw RV	-	50	-0.45	-0.45	0.63	0.51	0.77	0.42
Cor RV	-	50	-0.01	0.01	0.33	0.27	0.33	0.67
Raw RC	M12C-Dop(S1 wind)	50	-0.52	-0.61	0.69	0.55	0.86	0.24
Cor RC	M12C-Dop(S1 wind)	50	-0.08	-0.20	0.36	0.31	0.37	0.50
Cor RC	Y19C-Dop(S1 wind)	50	-0.15	-0.19	0.26	0.22	0.30	0.76
Cor RC	Y19C-Dop(ERA5 wind)	50	-0.16	-0.18	0.27	0.24	0.31	0.75
Cor RC	Y19C-Dop(Hereon waves)	50	-0.11	-0.08	0.24	0.20	0.26	0.83
Cor RC	Y19C-Dop(ERA5 waves)	50	-0.08	-0.05	0.23	0.20	0.25	0.84

(C) MEDIAN over BOX East

S1	WASV	*N*	mean	median	std	mad	rms	*r*
Raw RV	-	50	-0.21	-0.27	0.65	0.54	0.67	0.47
Cor RV	–	50	0.14	0.16	0.32	0.27	0.34	0.76
Raw RC	M12C-Dop(S1 wind)	50	-0.20	-0.33	0.66	0.51	0.69	0.40
Cor RC	M12C-Dop(S1 wind)	50	0.14	0.07	0.36	0.30	0.38	0.68
Cor RC	Y19C-Dop(S1 wind)	50	0.07	0.02	0.31	0.26	0.32	0.78
Cor RC	Y19C-Dop(ERA5 wind)	50	0.05	0.03	0.32	0.26	0.32	0.77
Cor RC	Y19C-Dop(Hereon waves)	50	0.06	0.08	0.26	0.21	0.26	0.90
Cor RC	Y19C-Dop(ERA5 waves)	50	0.09	0.11	0.24	0.20	0.26	0.93

dataset are shown as Supplementary Material in Fig. A.7 and Fig. A.8. Table 1 presents the statistical comparisons of the S1 radial velocities and radial currents obtained with different corrections against the collocated HF radar data. All comparisons are done with the HF radar current component in the S1 line-of-sight.

4.1. Pixel-to-pixel and median comparisons across the domain

Table 1A presents the results for S1 corrected radial currents using Y19C-Dop(ERA5 waves) to correct the WASV. Over the full domain, the dataset contains 551,725 individual valid match-up pixels, each with a native spatial resolution $\approx 0.7 \times 0.9\ km^2$. At pixel-to-pixel level, the statistics show zero bias, a standard deviation (std) and root-mean-square (rms) differences of 0.29 m/s and a correlation (r) of 0.73 (Table 1A, row 1).

Given the heterogeneous conditions over the region (e.g. bathymetry) and non-uniform density of HF radar data across the domain, two boxes denoted '954' and 'East' are selected for further analysis. Each box is 30 × 30 pixels in azimuth and range, corresponding to approximately $21 \times 27\ km^2$. The boxes are positioned where the number of match-ups is largest, close to in situ stations, and broadly representing 'offshore' and 'inshore' conditions (Fig. 2A). At pixel-to-pixel level, the statistics within each box (each containing ≈40,000 points) are slightly better than over the full domain, except for a small negative (positive) bias at Box 954 (East). Box 954, located further offshore, gives the best std (0.25 m/s) and better correlation ($r = 0.80$), whilst Box East shows even greater correlation ($r = 0.83$) but slightly degraded std (0.30 m/s), possibly due to greater dynamic range close to land (Table 1A, rows 2–3).

Since the boxes correspond to relatively uniform areas, the analyses proceed now using only median values over those boxes. The impact on statistics of using median values is small (Table 1A, rows 4–5). Using medians drastically reduces the number of match-ups (down to 50), but slightly improves both std and correlation in both Box 954 (std = 0.23 m/s, $r = 0.84$) and Box East (std = 0.24 m/s, $r = 0.93$). We get 50 match-ups instead of the expected 56 S1 collocated snapshots against HF radar, because HF radar does not cover the full domain for all acquisitions (see Fig. A.8). Biases remain unchanged, leaving a small negative bias offshore (Box 954, median = −0.05 m/s) and positive bias closer to land (Box East, median = 0.11 m/s).

4.2. Impact of proposed corrections

The statistics in each box are now examined for different radial velocity or current products and different corrections. Scatter plots between S1 products and HF radar data in Box 954 and East are presented in Fig. 4 with statistics reported in Table 1B and C.

In Fig. 4, the original operational S1 Level-2 RVL (empty circles) are shown against the collocated HF radar current in the S1 line-of-sight. Empty triangles correspond to the uncorrected S1 radial current, where only the WASV correction has been applied (here using M12C-Dop with S1 winds as input) but no instrument or platform corrections. The statistics of these 'Raw RV' and 'Raw RC' are shown in row 1 and 3 of Table 1B and 1C. Both products show large scatter and large biases against the HF radar measurements. Precision is poor (~0.6 m/s) and correlation is low (<0.5). This poor performance of the operational

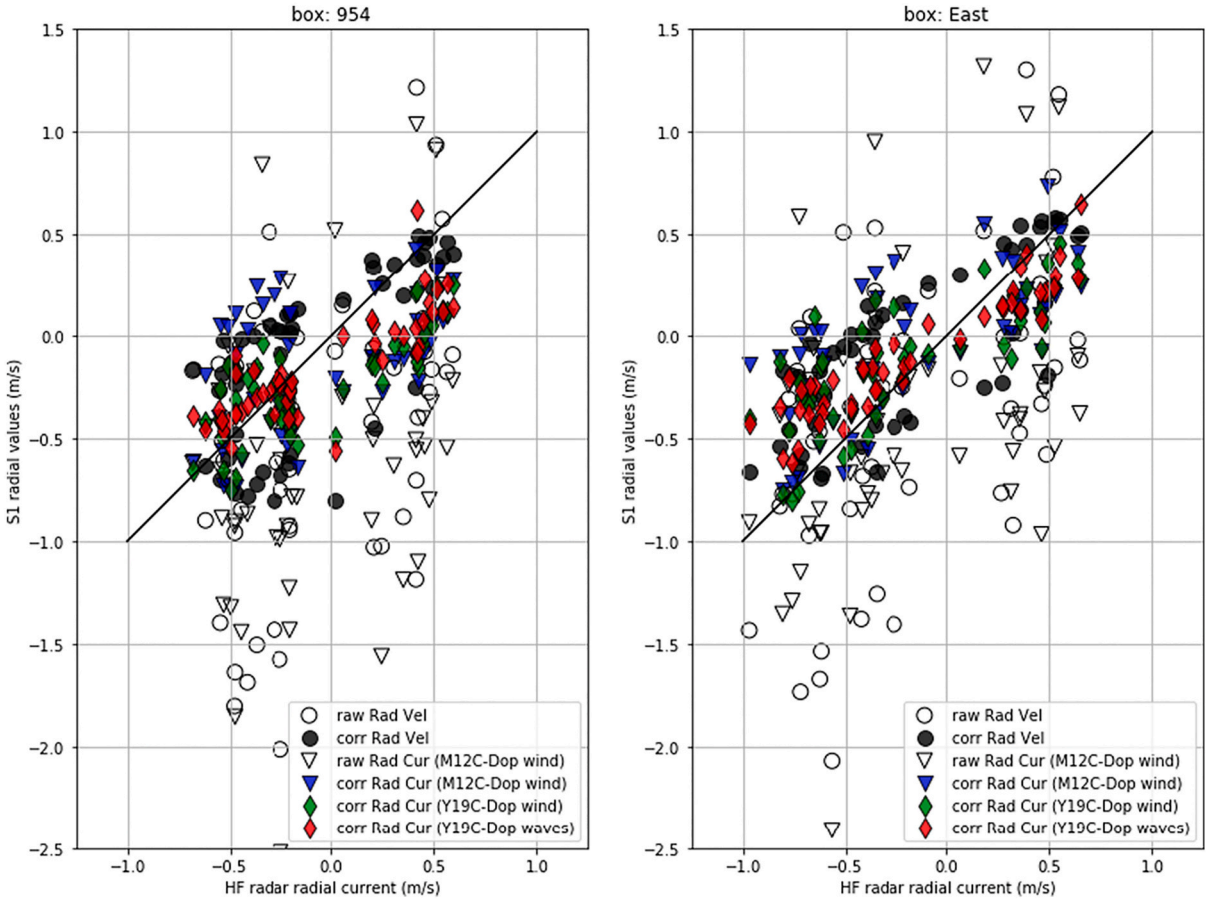

Fig. 4. Scatter plot of median S1 radial velocity or current with different corrections against HF radar current in the S1 line-of-sight. Left and right subplots show median values calculated over the 954 and East boxes (Fig. 2A). The meaning of different symbols is given in the legend. (For interpretation of the references to color in the text, the reader is referred to the web version of this article.)

S1 RVL products against HF radar is not surprising given the large non-geophysical errors reported in the previous section. Note that applying only the WASV does not improve the agreement with HF radar. In fact, on its own, the WASV causes larger errors (std >0.65 m/s) and worse correlation ($r < 0.4$). If Sentinel-1A data were well-calibrated, the WASV would be the only correction needed to obtain S1 radial currents that can be compared with HF radar data.

Let us now examine the impact of applying the proposed instrument and satellite corrections, but no WASV. Applying our scalloping and land-based corrections to the operational RVL results in corrected radial velocities ('cor RV') that show much better agreement with HF radar data (filled black circles in Fig. 4 and row 2 in Table 1B and 1C) with std $\sim$ 0.32 m/s and $r \sim 0.7$. The corrections remove RVL biases very effectively offshore (Box 954 median = 0.01 m/s) but less well closer to land (Box East median = 0.16 m/s).

If we now apply the WASV correction as well (using M12C-Dop with S1 winds as input; blue down-pointing triangles in Fig. 4; row 4 in Table 1B and 1C), the overall statistics of the Corrected RC ('cor RC') are – surprisingly – slightly worse (std $\sim$ 0.36 m/s, $r \sim 0.6$), particularly offshore. The WASV reduces the bias in Box East (median = 0.07 m/s) but introduces a large negative bias in Box 954 (median = −0.2 m/s). This unexpected deterioration suggests a possible issue with the WASV model or the input used to drive it. The next section considers in more detail how the choice of WASV computation affects S1 performance.

4.3. Impact of WASV correction

Table 1B and 1C rows 4–8 present the statistics against HF radar data obtained when calculating the WASV with M12C-Dop or Y19C-Dop and different wind or sea state input. Considering first the two WASV models driven with the same wind (S1 wind), rows 4–5 indicate much better performance with Y19C-Dop (std $\sim$ 0.29 m/s, $r \sim 0.77$) compared to M12C-Dop (std ~0.36 m/s, $r \sim 0.6$), particularly in Box 954. Y19C-Dop (S1 winds) reduces the median bias slightly in Box East (from 0.07 to 0.02 m/s) but leaves the large negative bias in Box 954 mostly unchanged (median ~−0.2 m/s).

Considering now only the Y19C-Dop WASV model with different input winds, rows 5–6 compare the results obtained with Y19C-Dop driven by S1 winds (Fig. 4, green diamonds) or ERA5 winds (not plotted). In both boxes, the results are mostly unchanged, with perhaps marginally better results with S1 winds.

Finally, we consider the impact of computing the WASV with sea state input instead of winds. The red diamonds in Fig. 4 represent Y19C-Dop(ERA5 waves) which gives the best results yet against HF radar data. The statistics in Table 1B and 1C (last row) confirm the significant improvements in precision (std $\sim$ 0.24 m/s) and correlation ($r > 0.84$). Our results are comparable to those of Moiseev et al. (2020a) who report 0.25 m/s RMSD against CODA HF radar at 5×5 km^2 based on six (6) S1A and S1B RVL acquisitions obtained with in-house L0 to Level-2 processing.

Improvements are particularly dramatic in Box East where the correlation reaches 0.93. This higher correlation at the coastal site could be explained by the stable precision and higher dynamic range of currents at this location. Nevertheless, there remain biases at both sites, around −0.05 m/s offshore (Box 954) but reaching +0.11 m/s closer to the coast (Box East). No improvement in performance is obtained (at any levels: pixel-to-pixel level, within boxes or at median box level) from using high-resolution wave information from the Hereon model as input to Y19C-Dop (Table 1B and C, row 7).

4.4. Independent assessment of S1 and ERA5 winds

Three marine weather stations in the study region [954; 2100; 102] provide in situ measurements of wind that can be used to independently assess the quality of the S1 and ERA5 wind data used as input to the WASV models. We focus primarily on wind direction since wind speed is a much weaker second-order effect in determining the magnitude of the WASV. Wind speed bias and precision for S1 and ERA5 are typically within 1.5 m/s at all stations.

Against stations 954 (UFS Deutsche Bucht; offshore), 2100 (Helgoland-Düne; inshore) and 102 (Leuchtturm Alte Weser; inshore), S1 wind direction shows mean biases of 0°, 7° and 5° and precisions (standard deviation) of 11°, 24° and 20° respectively. ERA5 gives very similar results for wind direction biases (1°, 7° and 5°) and slightly better precisions (9°, 16°, 17°). We note that the wind direction biases and precisions are better offshore (954) than inshore (2100, 102) for both S1 and ERA5. Unfortunately, in situ wind direction data are rounded to the nearest ten (10) degrees, making it difficult to provide more detailed analyses, particularly for biases.

4.5. Coastal jets and bathymetry

The dataset of 78 S1A passes over German Bight is now combined in time using a quadratic mean to construct the mean radial current field observed by S1 over the December 2017–July 2020 period. Fig. 5 shows the ~1 km resolution mean current field derived from S1 side-by-side with a high-resolution map of bathymetry of the region.

Focusing first on the eastern coastal boundary of the S1 domain, intense current jets are clearly visible close to the locations of deep bathymetry channels between islands and sand banks. The S1 current field provides remarkably detailed mapping of the complex fine-scale current jets in the area, including some associated with the Elbe river outflow.

On the southern coastal boundary of the domain, the coastal jets are less well defined. In this area, tidal currents run perpendicular to the S1 line-of-sight and will therefore have only weak components in the S1 radial direction (approximately East-West). Small exceptions include some of the channels associated with the Weser river due to their slanted orientation towards the S1 line-of-sight direction.

Fig. 5B also shows that the S1 mean field remains strongly impacted by residual signatures of the S1 TOPS scalloping, particularly in the middle sub-swath, but also in the eastern sub-swath where the scalloping anomalies partly mask coastal current features. This residual scalloping pattern can be traced back to substantial anomalies in a small number of S1 passes (see Fig. A.7) that are strong enough to impact the whole dataset. The presence of residual scalloping indicates that the simple correction proposed in this paper does not completely mitigate this effect. Further refinements should be envisaged to better handle these intermittent instrument anomalies.

The high-resolution S1 map in Fig. 5B represents the mean current in the S1 line-of-sight averaged over 2.5 years. In principle, the coastal current jets seen in the mean radial current should be detectable in the instantaneous S1 maps (see Fig. A.7), and such data could be extremely useful for coastal modelling and applications. But this is not possible at present due to the large anomalies and noise still present in some single-pass observations.

5. Discussion

5.1. Empirical corrections

Section 3.2 presented a number of empirical corrections proposed to mitigate the impact of Sentinel-1A platform errors and instrument anomalies on RVL data. These corrections were developed by examining the characteristics of S1A anomalies in 78 scenes obtained with the exact same geometry every 12 days over 2.5 years (Fig. 1).

The first and most obvious artefact in RVL images is the scalloping in azimuth that modulates RVL with an amplitude of the order of 0.1 m/s. This is a well-known effect of the TOPS acquisition mode and it is addressed in the operational processing from IPF 3.30 onwards. Meanwhile, our results show that the scalloping modulation is relatively constant in time, making it easy to estimate to provide a correction that

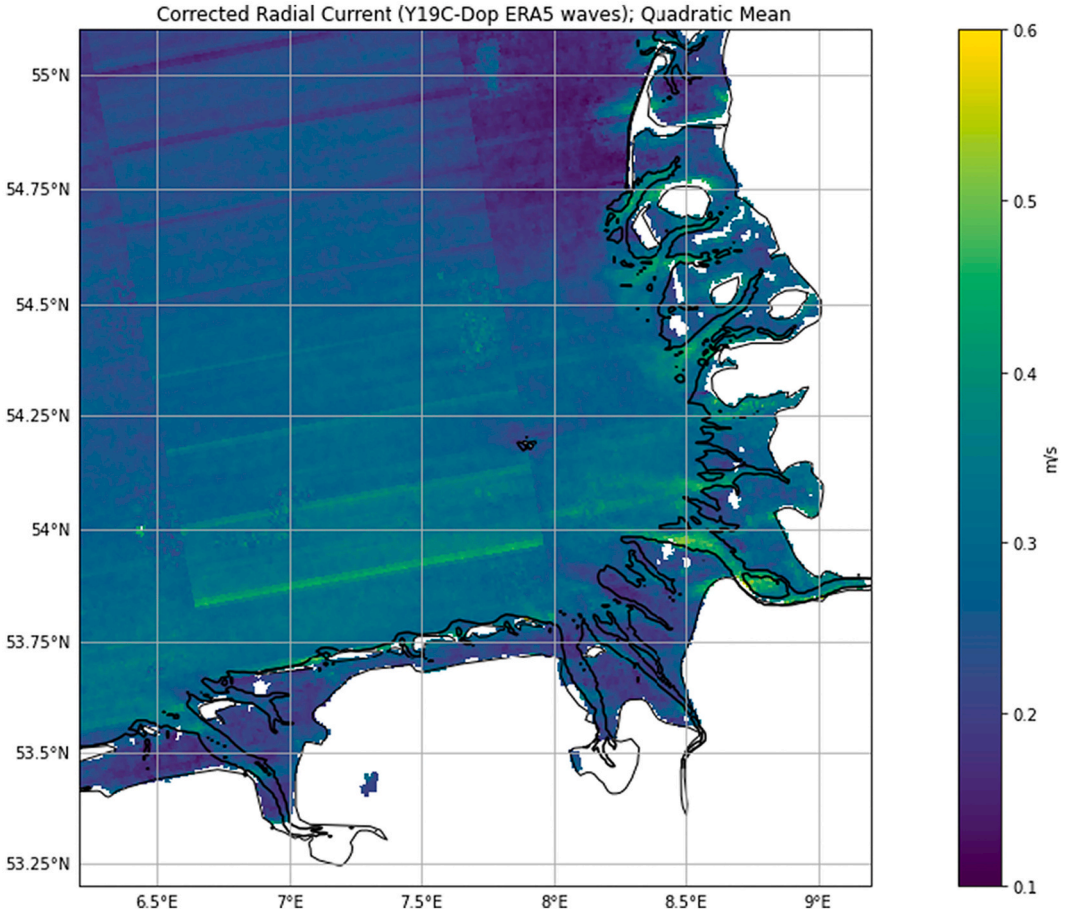

Fig. 5. Zoomed-in view of German Bight. S1 multi-pass averaged radial current (Y19C-Dop(ERA5 waves) WASV), showing intense current jets over deep bathymetry channels. Note residual banding in middle swath due to incomplete removal of S1 scalloping effect. The black line represent a 5 m deep contour line from high-resolution bathymetry (www.easygsh-db.org) with deep channels through coastal mud flats.

can be applied to all Sentinel-1A data. Our results also show that, after correcting the time-invariant component, there remain some small residual oscillations, indicating that the scalloping is changing slightly with time. This is particularly noticeable in the middle swath and could be a sign of slow instrument or antenna degradation. One way round this issue could be to compute this empirical correction regularly through the lifetime of the mission. For Sentinel-1B, the instrument uses the same TOPS acquisition technique as S1A, so a similar approach could be used to estimate and mitigate scalloping in S1B.

Next, our analyses revealed a dependence of RVL with range (across-track), different for the three sub-swaths, but broadly constant in each sub-swath across all 78 S1A cases. Relative to the mean RVL in each scene, RVL data are biased between −0.4 m/s (near range) and +0.1 m/s (far range). Once again, because this relative bias is consistent in time, the correction could be estimated and be applied to all Sentinel-1A data for both ascending and descending passes. The correction might evolve with time due to instrument or antenna degradation, but could again be estimated at regular intervals. The S1A range correction is unlikely to be directly applicable to Sentinel-1B, but the same approach could be used for S1B.

In contrast, the dependence of relative RVL with azimuth showed only limited consistency between the 78 S1A snapshots. The relative RVL varies with azimuth within ±0.2 m/s and the dependence is not sufficiently similar between scenes to compute a one-off time-invariant correction that can be applied to all overpasses. These variations are believed to originate from residual S1A platform attitude errors. With no access to accurate attitude information and corrections, our approach uses land as a calibration target to define zero motion. For this, S1 scenes need to image land in the along-track direction in one of the sub-swaths. The correction, estimated as a function of azimuth, can then be applied to the full image across all three sub-swaths.

At this point, it emerged that the (absolute) median RVL for each scene still displayed large temporal fluctuations across the 78 S1A overpasses. We find that the S1A median RVL over land — which should ideally give values close to zero — varies between −2.0 m/s and 0.8 m/s over the 2.5 years of the S1A dataset. Computing the median RVL over land pixels gives the absolute bias correction to be applied to each scene. Results suggest this bias correction changes relatively slowly in time, with a possible seasonal signature that may also depend on latitude. Only a small area of land is needed in the image to estimate this absolute bias correction. For scenes without land, it may be possible to estimate the correction by interpolation from neighbouring scenes, although this would need to be confirmed with further study.

Lastly, even after all these corrections, there are still occasional, unexplained, strong jumps in S1A RVL (several tens of cm/s). These occur across bursts and for integer numbers of scalloping oscillations and may be linked to S1 on-board temperature compensation (Hajduch et al., 2021). These strong events will affect the S1 retrieved current statistics and could explain some of the large errors observed in some cases. In the absence of flags in the operational products to identify and disregard these events, further investigations are needed to develop appropriate flagging methods.

All together, the empirical corrections bring significant improvements to S1A Level RVL data, resulting in higher quality RVL images and better quantitative agreement with HF radar data. Even without wave bias correction (next section), the empirical corrections reduce the S1

bias by almost 0.5 m/s, the standard deviation by about 0.3 m/s and increase the correlation with HF radar data from ~0.45 to ~0.71 (row 1–2 in Table 1B and C). Subsequent application of the wave bias correction (WASV) brings further improvements, as discussed in the next section.

5.2. Estimating the wind-wave artefact surface velocity bias

In Section 4.3, we evaluated the WASV correction by comparing the accuracy of S1A retrieved currents against HF radar data for two well-known WASV models by Mouche et al. (2012)(M12C-Dop) and Yurovsky et al. (2019) (Y19C-Dop). Traditionally, the WASV is expressed as a function of the wind vector, but here, we also examined the accuracy of S1A currents when calculating the WASV as a function of sea state. Two notable outcomes of our analyses are that, surprisingly, the widely-used M12C-Dop model degrades the S1A retrieved currents in this region; and using sea state as input to the WASV instead of wind vector gives much better results. In what follows, we first discuss the quality of the wind data and its influence on the WASV estimation, before examining in greater detail the differences between M12C-Dop and Y19C-Dop, and between wind vector and sea state WASV estimations.

5.2.1. Influence of wind accuracy on the WASV

Section 4.4 presented a brief assessment of the wind vector information from ERA5 and S1A that we used to estimate the WASV. ERA5 and S1 winds were compared against collocated independent in situ observations from weather stations in offshore and onshore parts of the region. The wind speed bias and precision were typically within 1.5 m/s and this was considered good enough for our purpose. Indeed, the sensitivity of the WASV to wind speed is relatively weak (not shown), a wind speed error of ~1.5 m/s corresponding to a difference in WASV less than 0.05 m/s for S1A IW range of incidence angles. Wind direction has a much greater impact on the WASV, as shown by the strong dependence of the WASV with relative wind direction in Fig. 6 for M12C-Dop (black dotted line) and Y19C-Dop (black solid line). The ERA5 and S1A wind direction bias and precision were typically within 15° of the in situ data. According to Fig. 6, a wind direction error of 15° can significantly impact the WASV, particularly when looking crosswind [30°–115°], when the difference in WASV exceeds 0.1 m/s and can reach up to 0.2 m/s.

In Section 4.4, we noted that ERA5 wind direction showed slightly better precision than S1 against in situ data. This did not translate into better precision in the S1 retrieved currents against the HF radar data however (Table 1B and 1C rows 5–6). Likewise, smaller biases in wind direction at the offshore station (954) for both ERA5 and S1 do not produce smaller biases in S1 currents against HF radar data. Thus, whilst better wind precision offshore is consistent with better S1 current precision obtained in Box 954, the uncertainties in S1 and ERA5 winds do not, by themselves, fully explain the errors observed in S1 radial currents against HF radar data.

5.2.2. Wind-driven WASV corrections and upwind/downwind asymmetry

One surprising finding is that applying the M12C-Dop WASV correction produces poorer accuracy in S1A retrieved currents against the HF radar data in this region (compare rows 2 and 4 in Table 1B and C). The corrected radial velocity (empirical corrections applied but no WASV) and corrected radial current (empirical corrections and M12C-Dop WASV applied) data are shown in Fig. 4 as black disks and down-pointing blue triangles respectively. These are shown also as separate subplots in Fig. A.9 (row 1 and 2) for clarity.

In Fig. 4, we note that the black disks describe two diagonal 'lines' on either side of the one-to-one line, albeit with shallower slopes. Closer examination indicates that the data above the $x = y$ line correspond predominantly to cases when S1A is looking downwind (westerly winds, from), whilst the data below the $x = y$ line correspond mostly to S1A looking upwind (easterly winds, from). This is also shown in Fig. A.9 where colours now refer to radar look direction relative to the wind (0° upwind, 180° downwind). Interestingly, each diagonal line is anchored at one end to the $x = y$ line, where corrected radial velocities agree well with HF radar data even without WASV correction. These clusters, seen more clearly in Fig. A.9 (row 1) are observed when S1A looks upwind (Easterlies) in ebbing flow (negative HF radar radial currents) and downwind (Westerlies) in flooding flow, both cases where wind and currents are aligned.

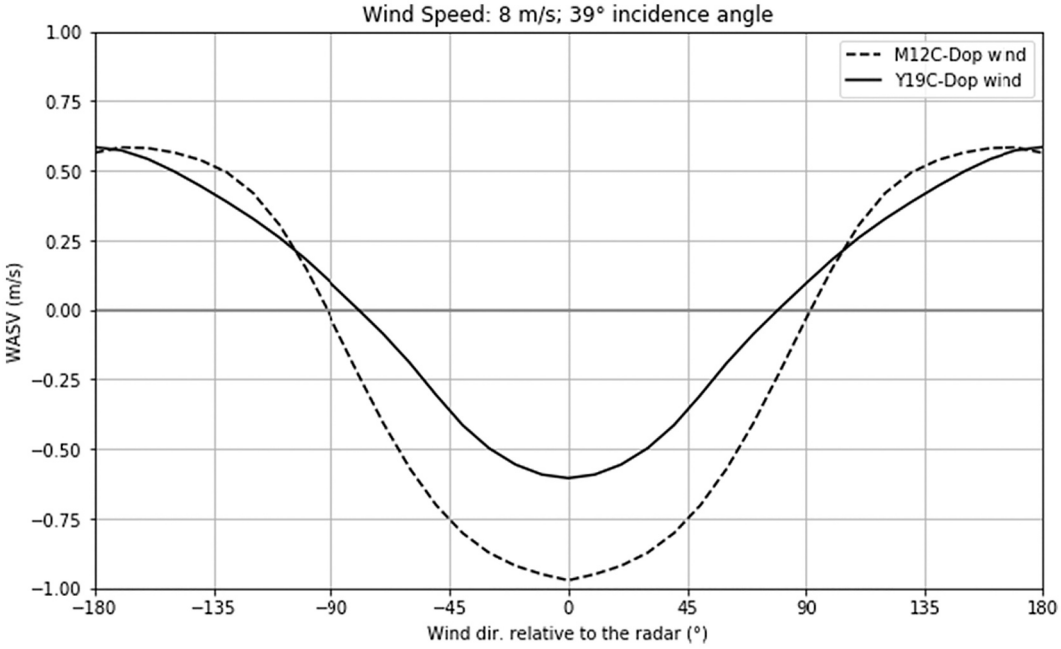

Fig. 6. Dependence of the Wind-wave Artefact Surface Velocity (WASV) on wind direction relative to the radar line-of-sight. 0° corresponds to the upwind direction. The WASV is calculated here for a wind speed of 8 m/s and incidence angle of 39° (S1 IW mid-swath) using (dashed) M12C-Dop and (solid) Y19C-Dop driven by fully developed sea state.

If the WASV model were perfect, the two diagonal 'lines' would both come closer to the $x = y$ line after applying the WASV. This is not the case here. Instead, when applying M12C-Dop, most upwind data move too far above the $x = y$ line and some downwind cases move too far below it. If we compare with Y19C-Dop (driven by the same wind input; green diamonds in Fig. 4, row 3 in Fig. A.9), the main difference is the better agreement with the HF radar data in upwind cases. This is consistent with the differences seen between the two models in Fig. 6 where M12C-Dop (black dotted line) and Y19C-Dop differ by almost 0.4 m/s within ±45° of the upwind direction.

From this, one could conclude that the M12C-Dop WASV correction is too strong in the upwind direction. Whereas the Y19C-Dop model presents a nearly symmetric sinusoidal dependence on relative wind direction, M12C-Dop has a strong upwind/downwind asymmetry that results in a much larger correction upwind. This strong upwind/downwind asymmetry was described by Mouche et al. (2012) based on Envisat-ASAR data in the open ocean, but was also reported by Martin et al. (2016) with airborne data in the coastal waters of Liverpool Bay/Irish Sea. In contrast, neither Yurovsky et al. (2019) (using Ka-band real aperture data in a coastal environment) nor Moiseev et al. (2020b) (using Sentinel-1B Wave mode data in open ocean conditions) found this asymmetry. The two later publications attribute this discrepancy to possible biases in M12C-Dop linked to remaining platform dependencies in Envisat ASAR, or to the impact of mixed seas.

At this point, we refrain from making definitive statements and leave this question open. The coastal conditions in this region are complex and some wind-current configurations are insufficiently sampled by the S1A data to allow us to be conclusive. Wind-current interactions when tides and wind align and short fetch when looking upwind are likely to play a role but these complex phenomena cannot be unravelled with this S1A dataset alone. Further research with more satellite data and other sites is needed to explore these issues and better understand and correct the WASV in coastal regions.

5.2.3. Driving Y19C-Dop with wind and/or sea state input

In Section 4.3, the best S1A radial current accuracy against HF radar data was obtained when correcting the WASV with the Y19C-Dop driven with sea state instead of wind. The improvement is particularly noticeable inshore (Box East). For convenience, Table 2 summarises the statistics of S1A radial currents against HF radar data when driving Y19C-Dop with wind or sea state. Here, all input data is from ERA5 for consistency.

Yurovsky et al. (2019) provide two formulations of the WASV, one a standard parameterization with wind vector — which assumes fully developed sea state as defined by Pierson and Moskowitz (1964) — and another with direct dependencies on wind sea and swell parameters. The best S1A radial current accuracy in Table 2 (row 3) corresponds to Y19C-Dop driven with ERA5 wave direction, wave height and peak frequency for both wind sea and swell. With full sea state, the S1A radial current precision reaches 0.23 m/s (std) and correlation with HF radar as high as 0.93. Contrast this with the S1A statistics obtained with wind vector, when precision and correlation are markedly worse (std ~0.3 m/s, $r \sim 0.76$). Using ERA5 windsea wave direction instead of ERA5 wind direction (row 1 and 2) brings no benefit, and in fact, results in a slight degradation of S1A radial currents against HF radar data. Fuller investigations of the relative impact of wind sea and swell in Y19C-Dop are underway but raise issues that cannot be comprehensively addressed in this paper, and will be the object of a future publication.

Table 2
Statistics of S1 radial currents versus HF radar for median values over Box 954 and Box East and different ERA5 wind and sea state input to the Y19C-Dop WASV model. Columns show: number of available samples (*N*); mean and median bias; standard deviation (std); median absolute deviation (mad); rms difference (rms); and Pearson correlation coefficient (*r*).

	N	mean	median	std	mad	rms	*r*
MEDIAN over BOX 954 using Y19C-Dop driven by:							
ERA5 wind dir &wind speed	50	-0.16	-0.18	0.27	0.24	0.31	0.75
ERA5 windsea dir &wind speed	50	-0.16	-0.13	0.28	0.25	0.32	0.71
ERA5 waves full (windsea &swell)	50	-0.08	-0.05	0.23	0.20	0.25	0.84
MEDIAN over BOX East using Y19C-Dop driven by:							
ERA5 wind dir &wind speed	50	0.05	0.03	0.32	0.26	0.32	0.77
ERA5 windsea dir &wind speed	50	0.06	0.02	0.32	0.27	0.33	0.76
ERA5 waves full (windsea &swell)	50	0.09	0.11	0.24	0.20	0.26	0.93

The beneficial impact of computing the WASV with sea state is most clearly visible in Fig. 4 (red diamonds) and the bottom subplots in Fig. A.9, where the application of the Y19C-Dop(ERA5 waves) WASV brings the S1A radial currents for all wind/current conditions closer to the $x = y$ line.

Both inshore and offshore, the S1A radial currents now follow a tight linear relation with the HF radar data, albeit one with a weaker slope than the $x = y$ line. The weaker slope reflects the slightly smaller dynamic range observed with S1A radial currents in both boxes compared to the HF radar. The fact that both locations show weaker linear relations with HF radar data indicate additional sensitivities that scale with the intensity of the radial current and could relate to unresolved dependencies in the WASV, or differences in the surface currents sensed by S1 and by the HF radar.

6. Conclusion and outlook

Sentinel-1A (S1A) radial velocity data were evaluated over an HF radar instrumented site in the German Bight over a 2.5 years period (December 2017–July 2020). Our analyses confirm the strong impact of uncorrected platform and instrument effects that prevent direct exploitation of operational Sentinel-1A Level-2 Ocean radial velocity products (RVL). Without mitigation of these effects, S1A radial velocities compare poorly against HF radar data with large root-mean-square differences (rms) around 0.7 m/s and correlations below 0.5.

The study used 78 S1A images obtained every 12 days over 2.5 years from ascending passes with the exact same viewing geometry to characterise and correct S1A platform and instrument artefacts. Empirical corrections were proposed that remove time-invariant effects and use land pixels in the images as calibration target to define zero motion. The largest errors in RVL are temporally fluctuating biases (estimated from land pixels where RVL should be close to zero) that impact the whole scene and vary between −2.0 m/s and 0.8 m/s over the 2.5 years of the S1A dataset. These fluctuations, thought to originate from uncorrected platform attitude effects, show a possible seasonal signature that may also depend on latitude.

All together, the empirical corrections bring significant improvements to S1A Level RVL data, resulting in higher quality RVL images and better quantitative agreement with HF radar data. The empirical corrections alone reduce the S1 bias by almost 0.5 m/s, the standard deviation by about 0.3 m/s and increase the correlation with HF radar data from ~0.45 to ~0.71. However, even after all these corrections, occasional, unexplained, strong S1A RVL jumps (several tens of cm/s) are still observed that could explain some of the large errors observed in some cases. Given the absence of flags in the operational products, further investigations are needed to develop appropriate flagging to identify and disregard these events in future analyses.

Subsequent application of the wave bias correction (WASV) brings further improvements to the accuracy of S1A radial currents against HF radar data. Best results were obtained in this region when computing the WASV with the Yurovsky et al. (2019) formulation, particularly when using sea state rather than wind vector as input. Accounting for sea state produces S1 radial currents with a precision (std) around 0.3 m/s at

~1 km resolution. Precision improves to ~0.24 m/s when averaging over 21 × 27 km^2, with correlations with HF radar data reaching up to 0.93. The WASV estimated by Mouche et al. (2012) results in poorer accuracy of S1A radial currents against HF radar data, possibly because of the large upwind/downwind asymmetry that may not hold in this region. However, evidence of wind-current interactions when tides and wind align and the short fetch when looking upwind make it difficult to be conclusive with this S1A data alone, calling for further research with more satellite data and other sites to explore these issues and better understand and correct the WASV in coastal regions.

Combining 2.5 years of S1A acquisitions produces maps of climatological S1A radial currents at 1 km resolution that reveal coastal current jets and fine details of the coastal circulation that closely match the known bathymetry and deep-water coastal channels in this region. In principle, coastal current jets could be detected also from single S1 overpasses, but this is not presently possible due to large anomalies and noise still observed in many S1 RVL images. In future, it may be worth building climatological maps of radial currents from ascending and descending passes to observe both components of the mean radial current in a given region. Given the time separation between ascending and descending passes (hours to days), one would combine the climatological mean (not the instantaneous radial currents) to obtain a full description of the mean total current vector field.

Sentinel-1A data confirm the wealth of oceanographic information contained in microwave Doppler signals. The global sampling and wide-swath coverage of satellites could complement and extend the observations of total surface current fields already provided by HF radars in some coastal regions. Although no satellite will ever match the high temporal sampling achievable with HF radars (hourly or better, typically), HF radar installations can be difficult to deploy and maintain in challenging and remote environments. They remain the preserve of mainly industrialised nations, leaving much of the world's coastal currents to have never been observed.

The results with S1A RVL are very promising and demonstrate the ability of microwave Doppler instruments to provide useful observations of total ocean surface currents at fine spatial scale right up to the coast. Regular satellite observations of coastal bathymetry and circulation would be of great interest and benefit for ocean observing and modelling in coastal regions. The work in this study should open new avenues of research and encourage greater exploitation of Sentinel-1 RVL data. Our findings are also directly relevant to two satellite missions currently under development as possible future Earth Explorer missions for the European Space Agency: the Harmony mission (ESA, 2020; Kleinherenbrink et al., 2020) and SEASTAR (Gommenginger et al., 2019). Both missions aim to provide maps of total ocean surface current vectors with single-pass acquisitions. Harmony comprises two passive satellites flying in formation with Sentinel-1 and seeks to produce instantaneous 2D maps of total ocean surface current vector at 25 km^2 spatial resolution and 0.2 m/s accuracy. In contrast, SEASTAR plans to deliver total surface current vectors with fine spatial resolution (1 km) and accuracy (0.1 m/s) to study small scale ocean dynamics and vertical exchanges between the atmosphere and the ocean interior, and to quantify, for the first time, these fast-evolving processes on daily to multi-annual scales, across different ocean conditions and latitudes, over all coastal and shelf seas and Marginal Ice Zones. Improved understanding of interactions between winds, waves and currents and their influence on the WASV in open ocean and coastal conditions remain a key question in order to help these missions achieve their stated observational objectives.

Credit author statement

Conceptualization: AM, CG; Data curation: AM, BJ; Formal aanalysis: AM, CG; Funding acquisition: AM, JS; Writing - original draft: AM; Writing - review & editing: AM, CG, BJ, JS.

Declaration of Competing Interest

The authors declare that they have no known competing financial interests or personal relationships that could have appeared to influence the work reported in this paper.

Acknowledgments

The present work was supported by data and funding from the H2020 CEASELESS project (grant agreement No. 730030) co-funded by strategic internal R&D funding from the National Oceanography Centre under national capability funding from the UK Natural Environment Research Council.

The authors would like to thank Meric Srokosz (NOC) for his helpful comments while discussing the results.

Appendix A. Supplementary data

Supplementary data to this article can be found online at https://doi.org/10.1016/j.rse.2021.112758.

References

Ardhuin, F., Brandt, P., Gaultier, L., Donlon, C., Battaglia, A., Boy, F., Casal, T., Chapron, B., Collard, F., Cravatte, S., Delouis, J.-M., De Witte, E., Dibarboure, G., Engen, G., Johnsen, H., Lique, C., Lopez-Dekker, P., Maes, C., Martin, A., Marié, L., Menemenlis, D., Nouguier, F., Peureux, C., Rampal, P., Ressler, G., Rio, M.-H., Rommen, B., Shutler, J.D., Suess, M., Tsamados, M., Ubelmann, C., van Sebille, E., van den Oever, M., Stammer, D., 2019. SKIM, a candidate satellite mission exploring global ocean currents and waves. Front. Mar. Sci. 6, 209. https://doi.org/10.3389/fmars.2019.00209.

Barth, A., Alvera-Azcárate, A., Gurgel, K.-W., Staneva, J., Port, A., Beckers, J.-M., Stanev, E., 2010. Ensemble perturbation smoother for optimizing tidal boundary conditions by assimilation of high-frequency radar surface currents, application to the German Bight. Ocean Sci. 6, 161–178.

Baschek, B., Brix, H., Badewien, T., Breitbach, G., Colijn, F., Doerffer, R., Emeis, K., Eschenbach, C., Friedrich, J., Fischer, P., et al., 2016. COSYNA: Coastal observing system for northern and arctic seas. Ocean Sci.

Baschek, B., Schroeder, F., Brix, H., Riethmüller, R., Badewien, T.H., Breitbach, G., Brügge, B., Colijn, F., Doerffer, R., Eschenbach, C., Friedrich, J., Fischer, P., Garthe, S., Horstmann, J., Krasemann, H., Metfies, K., Merckelbach, L., Ohle, N., Petersen, W., Pröfrock, D., Röttgers, R., Schlüter, M., Schulz, J., Schulz-Stellenfleth, J., Stanev, E., Staneva, J., Winter, C., Wirtz, K., Wollschläger, J., Zielinski, O., Ziemer, F., 2017. The coastal observing system for northern and arctic seas (COSYNA). Ocean Sci. 13, 379–410. https://doi.org/10.5194/os-13-379-2017.

Bourbigot, M., Vincent, P., Johnsen, H., Piantanida, R., 2020. Sentinel-1 IPF Auxiliary Product Specification. Technical Report ESA S1-RS-MDA-52-7443. https://sentinel.esa.int/documents/247904/1877131/Sentinel-1_IPF_Auxiliary_Product_Specification.

Hagen, R., Freund, J., Plüß, A., Ihde, R., 2019. In: Bundesanstalt für Wasserbau (Ed.), Validierungsdokument easygsh-db nordseemodell. teil: Untrim2 – sedimorph – unk. https://doi.org/10.18451/K2_EASYGSH_1. https://mdi-de.baw.de/easygsh/assets/Dokumente/Veroeffentlichungen/Validierungsdokument_EasyGSH_DB_Nordseemodell.pdf.

Chapron, B., Collard, F., Ardhuin, F., 2005. Direct measurements of ocean surface velocity from space: interpretation and validation. J. Geophys. Res. Oceans 110. https://doi.org/10.1029/2004JC002809.

De Zan, F., Monti Guarnieri, A., 2006. TOPSAR: Terrain observation by progressive scans. IEEE Trans. Geosci. Remote Sens. 44, 2352–2360. https://doi.org/10.1109/TGRS.2006.873853.

ESA, 2020. Report for Assessment: Earth Explorer 10 Candidate Mission Harmony. ESA-EOPSM-HARM-RP-3784 European Space Agency Noordwijk, The Netherlands.

Fois, F., Hoogeboom, P., Le Chevalier, F., Stoffelen, A., 2015. An analytical model for the description of the full polarimetric sea surface Doppler signature. J. Geophys. Res. Oceans. https://doi.org/10.1002/2014JC010589.

Goldstein, R., Zebker, H., 1987. Interferometric radar measurement of ocean surface currents. Nature 328, 707–709.

Gommenginger, C., Chapron, B., Hogg, A., Buckingham, C., Fox-Kemper, B., Eriksson, L., Soulat, F., Ubelmann, C., Ocampo-Torres, F., Nardelli, B.B., Griffin, D., Lopez-Dekker, P., Knudsen, P., Andersen, O., Stenseng, L., Stapleton, N., Perrie, W., Violante-Carvalho, N., Schulz-Stellenfleth, J., Woolf, D., Isern-Fontanet, J., Ardhuin, F., Klein, P., Mouche, A., Pascual, A., Capet, X., Hauser, D., Stoffelen, A., Morrow, R., Aouf, L., Breivik, Ø., Fu, L.-L., Johannessen, J.A., Aksenov, Y., Bricheno, L., Hirschi, J., Martin, A.C.H., Martin, A.P., Nurser, G., Polton, J., Wolf, J., Johnsen, H., Soloviev, A., Jacobs, G.A., Collard, F., Groom, S., Kudryavtsev, V., Wilkin, J., Navarro, V., Babanin, A., Martin, M., Siddorn, J., Saulter, A., Rippeth, T., Emery, B., Maximenko, N., Romeiser, R., Graber, H., Azcarate, A.A., Hughes, C.W., Vandemark, D., Silva, J.d., Leeuwen, P.J.V., Naveira-Garabato, A., Gemmrich, J., Mahadevan, A., Marquez, J., Munro, Y., Doody, S., Burbidge, G., 2019. SEASTAR: a

mission to study ocean submesoscale dynamics and small-scale atmosphere-ocean processes in coastal, shelf and polar seas. Front. Mar. Sci. 6, 457. https://doi.org/10.3389/fmars.2019.00457.

Group, T.W., 1988. The WAM model, a third generation ocean wave prediction model. J. Phys. Oceanogr. 18, 1775–1810. https://doi.org/10.1175/1520-0485(1988)018<1775:TWMTGO>2.0.CO;2. https://journals.ametsoc.org/view/journals/phoc/18/12/1520-0485_1988_018_1775_twmtgo_2_0_co_2.xml.

Gurgel, K.-W., Antonischki, G., Essen, H.-H., Schlick, T., 1999. Wellen radar (WERA): a new ground-wave HF radar for ocean remote sensing. Coast. Eng. 37, 219–234. https://doi.org/10.1016/s0378-3839(99)00027-7.

Hajduch, G., Vincent, P., Piantanida, R., Recchia, A., Franceschi, N., Schmidt, K., Johnsen, H., Mouche, A., Grouazel, A., Collard, F., Guitton, G., 2021. Sentinel-1 A and B Annual Performance Report for 2020. DI-MPC-APR MPC-0504 European Union/ESA – Copernicus. https://sentinel.esa.int/documents/247904/4607145/Sentinel-1-Annual-Performance-Report-2020.pdf/1eac12a7-26ca-002c-b3ff-78f6a1d77653.

Hansen, M.W., Johannessen, J.A., Dagestad, K.F., Collard, F., Chapron, B., 2011. Monitoring the surface inflow of Atlantic Water to the Norwegian Sea using Envisat ASAR. J. Geophys. Res. Oceans 116. https://doi.org/10.1029/2011JC007375 n/a-n/a.

Hersbach, H., Bell, B., Berrisford, P., Hirahara, S., Horányi, A., Muñoz-Sabater, J., Nicolas, J., Peubey, C., Radu, R., Schepers, D., Simmons, A., Soci, C., Abdalla, S., Abellan, X., Balsamo, G., Bechtold, P., Biavati, G., Bidlot, J., Bonavita, M., De Chiara, G., Dahlgren, P., Dee, D., Diamantakis, M., Dragani, R., Flemming, J., Forbes, R., Fuentes, M., Geer, A., Haimberger, L., Healy, S., Hogan, R.J., Hólm, E., Janisková, M., Keeley, S., Laloyaux, P., Lopez, P., Lupu, C., Radnoti, G., de Rosnay, P., Rozum, I., Vamborg, F., Villaume, S., Thépaut, J.-N., 2020. The ERA5 global reanalysis. Q. J. R. Meteorol. Soc. 146, 1999–2049. https://doi.org/10.1002/qj.3803.

Johannessen, J.A., Chapron, B., Collard, F., Kudryavtsev, V., Mouche, A., Akimov, D., Dagestad, K.-F., 2008. Direct ocean surface velocity measurements from space: improved quantitative interpretation of Envisat ASAR observations. Geophys. Res. Lett. 35 https://doi.org/10.1029/2008GL035709.

Kleinherenbrink, M., Korosov, A., Newman, T., Theodosiou, A., Li, Y., Mulder, G., Rampal, P., Stroeve, J., Lopez-Dekker, P., 2020. Estimating instantaneous sea-ice dynamics from space using the bi-static radar measurements of Earth Explorer 10 candidate Harmony. Cryosph. Discuss. 2020, 1–25. https://doi.org/10.5194/tc-2020-245. https://tc.copernicus.org/preprints/tc-2020-245/.

Martin, A.C.H., Gommenginger, C., Marquez, J., Doody, S., Navarro, V., Buck, C., 2016. Wind-Wave induced velocity in ATI SAR Ocean Surface Currents: first experimental evidence from an airborne campaign. J. Geophys. Res. Oceans. https://doi.org/10.1002/2015JC011459.

Milbradt, P., Valerius, J., Zeiler, M., 2015. Das Funktionale Bodenmodell: Aufbereitung einer Konsistenten Datenbasis für die Morphologie und Sedimentologie. Die Küste, 83 AufMod, pp. 19–38.

Moiseev, A., Johnsen, H., Hansen, M., Johannessen, J., 2020a. Evaluation of radial ocean surface currents derived from sentinel-1 iw doppler shift using coastal radar and lagrangian surface drifter observations. J. Geophys. Res. Oceans. https://doi.org/10.1029/2019JC015743 e2019JC015743.

Moiseev, A., Johnsen, H., Johannessen, J.A., Collard, F., Guitton, G., 2020b. On removal of sea state contribution to sentinel-1 doppler shift for retrieving reliable ocean surface current. J. Geophys. Res. Oceans 125. https://doi.org/10.1029/2020JC016288 e2020JC016288 E2020JC016288 2020JC016288.

Mouche, A., Collard, F., Chapron, B., Dagestad, K., Guitton, G., Johannessen, J., Kerbaol, V., Hansen, M., 2012. On the use of Doppler shift for sea surface wind retrieval from SAR. IEEE Trans. Geosci. Remote Sens. 50 https://doi.org/10.1109/TGRS.2011.2174998.

Mouche, A.A., Vincent, P., Hajduch, G., 2019. Sentinel-1 Ocean Wind Fields (OWI) Algorithm Definition. S1-TN-CLS-52-9049, DI-MPC-IPFDD, MPC-0455 ESA – CLS. https://sentinels.copernicus.eu/documents/247904/3861173/Sentinel-1-Ocean-Wind-Fields-OWI-ATBD.pdf.

Nouguier, F., Guerin, C., Soriano, G., 2011. Analytical techniques for the Doppler signature of sea surfaces in the microwave regime I: Linear surfaces. IEEE Trans. Geosci. Remote Sens. 49, 4856–4864. https://doi.org/10.1109/TGRS.2011.2152848.

Pierson, W., Moskowitz, L., 1964. A proposed spectral form for fully developed wind seas based on the similarity theory of S.A. Kitaigorodskii. J. Geophys. Res. 69, 5181–5190. https://doi.org/10.1029/JZ069i024p05181. http://www.agu.org/pubs/crossref/1964/JZ069i024p05181.shtml.

Plant, W.J., Alpers, W., 1994. An introduction to SAXON-FPN. J. Geophys. Res. Oceans 99, 9699–9703. https://doi.org/10.1029/93JC03482.

Rodríguez, E., Bourassa, M., Chelton, D., Farrar, J.T., Long, D., Perkovic-Martin, D., Samelson, R., 2019. The winds and currents mission concept. Front. Mar. Sci. 6, 438. https://doi.org/10.3389/fmars.2019.00438.

Rodriguez-Cassola, M., Prats-Iraola, P., De Zan, F., Scheiber, R., Reigber, A., Geudtner, D., Moreira, A., 2015. Doppler-related distortions in TOPS SAR images. IEEE Trans. Geosci. Remote Sens. 53, 25–35. https://doi.org/10.1109/TGRS.2014.2313068.

Romeiser, R., Runge, H., Suchandt, S., Kahle, R., Rossi, C., Bell, P., 2014. Quality assessment of surface current fields from TerraSAR-X and TanDEM-X along-track interferometry and Doppler centroid analysis. IEEE Trans. Geosci. Remote Sens. 52, 2759–2772. https://doi.org/10.1109/TGRS.2013.2265659.

Romeiser, R., Suchandt, S., Runge, H., Steinbrecher, U., Grünler, S., 2010. First analysis of TerraSAR-x along-track insar-derived current fields. IEEE Trans. Geosci. Remote Sens. 48, 820–829. https://doi.org/10.1109/TGRS.2009.2030885.

Romeiser, R., Thompson, D., 2000. Numerical study on the along-track interferometric radar imaging mechanism of oceanic surface currents. IEEE Trans. Geosci. Remote Sens. 38, 446–458. https://doi.org/10.1109/36.823940.

Rouault, M.J., Mouche, A., Collard, F., Johannessen, J.A., Chapron, B., 2010. Mapping the agulhas current from space: an assessment of ASAR surface current velocities. J. Geophys. Res. Oceans 115, C10026. https://doi.org/10.1029/2009JC006050.

Rufenach, C.L., Shuchman, R.A., Lyzenga, D.R., 1983. Interpretation of synthetic aperture radar measurements of ocean currents. J. Geophys. Res. Oceans 88, 1867–1876. https://doi.org/10.1029/JC088iC03p01867.

Shuchman, R.A., Meadows, G.A., 1980. Airborne synthetic aperture radar observation of surf zone conditions. Geophys. Res. Lett. 7, 857–860. https://doi.org/10.1029/GL007i011p00857.

Stanev, E.V., Ziemer, F., Schulz-Stellenfleth, J., Seemann, J., Staneva, J., Gurgel, K.-W., 2015. Blending surface currents from HF radar observations and numerical modeling: tidal hindcasts and forecasts. J. Atmos. Ocean. Technol. 32, 256–281. https://doi.org/10.1175/jtech-d-13-00164.1.

Staneva, J., Grayek, S., Behrens, A., Günther, H., 2021. GCOAST: skill assessments of coupling wave and circulation models (NEMO-WAM). J. Phys. Conf. Ser. 1730, 012071. https://doi.org/10.1088/1742-6596/1730/1/012071.

Stewart, R.H., Joy, J.W., 1974. Hf radio measurements of surface currents. Deep Sea Res. 21, 1039–1049.

Teague, C., Vesecky, J., Hallock, Z., 2001. A comparison of multifrequency HF radar and ADCP measurements of near-surface currents during COPE-3. IEEE J. Ocean. Eng. 26, 399–405. https://doi.org/10.1109/48.946513.

Torres, R., Snoeij, P., Geudtner, D., Bibby, D., Davidson, M., Attema, E., Potin, P., Rommen, B., Floury, N., Brown, M., Traver, I.N., Deghaye, P., Duesmann, B., Rosich, B., Miranda, N., Bruno, C., L'Abbate, M., Croci, R., Pietropaolo, A., Huchler, M., Rostan, F., 2012. GMES Sentinel-1 mission. Remote Sens. Environ. 120, 9–24. https://doi.org/10.1016/j.rse.2011.05.028. http://www.sciencedirect.com/science/article/pii/S0034425712000600.

Wiese, A., Staneva, J., Schulz-Stellenfleth, J., Behrens, A., Fenoglio-Marc, L., Bidlot, J.-R., 2018. Synergy of wind wave model simulations and satellite observations during extreme events. Ocean Sci. 14, 1503–1521. https://doi.org/10.5194/os-14-1503-2018.

Yurovsky, Y.Y., Kudryavtsev, V.N., Grodsky, S.A., Chapron, B., 2019. Sea surface Ka-band doppler measurements: analysis and model development. Remote Sens. 11 https://doi.org/10.3390/rs11070839. http://www.mdpi.com/2072-4292/11/7/839.